ELSEVIER

Contents lists available at ScienceDirect

Applied Catalysis B: Environmental

journal homepage: www.elsevier.com/locate/apcatb





Atomic-layer Fe₂O₃-modified 2D porphyrinic metal-organic framework for enhanced photocatalytic disinfection through electron-withdrawing effect

Jun Li ^a, Zhenduo Cui ^a, Yufeng Zheng ^b, Xiangmei Liu ^c, Zhaoyang Li ^a, Hui Jiang ^a, Shengli Zhu ^a, Yu Zhang ^d, Paul K. Chu ^e, Shuilin Wu ^{a,b,*}

- ^a The Key Laboratory of Advanced Ceramics and Machining Technology by the Ministry of Education of China, School of Materials Science & Engineering, Tianjin University, Tianjin 300072, China
- b School of Materials Science & Engineering, Peking University, Beijing 100871, China
- c School of Life Science and Health Engineering, Hebei University of Technology, Xiping Avenue 5340, Beichen District, Tianjin 300401, China
- d Department of Orthopedics, Guangdong Provincial People's Hospital, Guangdong Academy of Medical Sciences, Guangzhou 510080, China
- ^e Department of Physics, Department of Materials Science and Engineering, and Department of Biomedical Engineering, City University of Hong Kong, Tat Chee Avenue, Kowloon 999077, Hong Kong, China

ARTICLE INFO

Keywords: 2D metal-organic framework Atomic layer deposition Electron-withdrawing Photocatalysis Disinfection

ABSTRACT

In this work, an atomic-layer Fe_2O_3 -modified two-dimensional (2D) porphyrinic metal-organic framework (MOF) was prepared (2D MOF- Fe_2O_3), which exhibits unique interfacial electron-withdrawing effect via charge transfer pathways from Zn_2O_8 and C-O bonds to Fe-O bonds. Concretely, the atomic-layer Fe_2O_3 is deposited on 2D porphyrinic MOF (ZnTCPP) by atomic layer deposition technique to enhance the photocatalytic performance and the subsequent bacteria-killing efficacy. After 20 min light irradiation, the photocatalytic antibacterial efficacy of 2D MOF- Fe_2O_3 can reach up to 99.9%. The underlying mechanism of enhanced photocatalytic activity is that the heterointerface between 2D MOF and Fe_2O_3 can facilitate the transfer of lots of photogenerated electrons from 2D MOF to Fe_2O_3 , where 2D MOF and Fe_2O_3 act as electronic donator and receptor, respectively. This work provides an insight into developing highly effective photocatalysts by using electron-withdrawing modulator to optimize charge transfer pathway.

1. Introduction

Photonic metal-organic frameworks (MOFs) possess the specific crystalline porous structures by sequential coordination of metal ions/clusters with organic linkers (including functional chromophores) [1,2]. The rational design by controllable and ordered arrangements of inorganic and organic photonic units can not only maintain their intrinsic optical properties of units, but also further improve their photonic functionality by the synergistic effect among multiple units [3–5]. Notably, porphyrin-based MOFs are one of the most widely used photonic MOFs because porphyrinic compounds are considered to be the most abundant and significant pigments in nature, and called as "pigments of life" [6]. Recently, porphyrinic MOFs have various functional applications, such as solar light-driven photocatalysts and biomedicines (such as biosensor, bioimaging, and photodynamic or photothermal therapy) [3,7]. Therefore, optimizing photonic functionality of

porphyrinic MOFs is very significant and promising.

Among various porphyrinic MOFs, 2D porphyrinic MOFs have many excellent features, including relatively large surface area, abundant catalytic active sites, outstanding light-harvesting network, and fast energy migration [8–10]. Besides, their 2D nanostructures with atomically thin nanosheets are beneficial for modifiable chemical functionality and tunable electronic structure by loading other photonic materials to achieve synergistic effect of photonic property [8,10,11]. However, the relatively rapid charge recombination rate in their metal-linker bridging units restricts better photocatalytic performance [7]. Notably, the key challenge of accurate selection and design of synergistic photonic units lies in understanding the mechanism of charge transfer of 2D photonic MOFs.

For charge transfer pathways in 2D photonic MOFs, ligand-to-metal charge transfer (LMCT) and metal-to-ligand charge transfer (MLCT) are the two most typical ways during transition from excited states to

E-mail address: slwu@pku.edu.cn (S. Wu).

^{*} Corresponding author at: The Key Laboratory of Advanced Ceramics and Machining Technology by the Ministry of Education of China, School of Materials Science & Engineering, Tianjin University, Tianjin 300072, China.

ground state [7,12,13]. In this electron donor-acceptor system, LMCT (partial electron transfer from ligand-localized orbitals to metal-localized orbitals) and MLCT (partial electron transfer from metal-localized orbitals to ligand-localized orbitals) favor prolonged lifetimes and low-recombination rates of photogenerated charges [13]. However, the limited efficiency of charge transfer and separation in 2D photonic MOF restricts their photocatalytic performance [7,14,15]. Regulating charge transfer pathway by modulating electronic structures is a promising prospect to optimize light-harvesting ability of metal-linker bridging units in 2D MOFs [10]. Especially, developing 2D photonic MOF-based heterointerfaces by surface engineering may offer an efficient strategy to promote their efficiency of charge transfer.

Atomic layer deposition (ALD) serving as a powerful surfaceengineered technique is able to prepare various nanomaterials through different precursors by alternating sequential deposition, including metal oxides, metal nitrides, metal phosphates, metal sulfides, and so on [16,17]. The thickness of ALD-grown nanofilm can be precisely controlled at atomic level by modulating the number of reaction cycles. Concretely, during gas-phase deposition process, self-limiting and saturated surface reactions can achieve accurate atomic-layer thickness control and excellent atomic-scale uniformity [16,17]. Therefore, ALD-engineered 2D photonic MOFs are expected to construct efficient and stable heterointerfaces at atomic layer level, thus improving their interfacial charge transfer, photonic functionality, and photocatalytic property. Notably, the atomically thin 2D metal oxides prepared by ALD possess unique electronic and optical properties, where the most representative candidates can serve as redox-active semiconducting photocatalysts, including TiO₂, Fe₂O₃, and ZnO [18,19]. Besides, they possess the excellent ability of photocatalytic reactive oxygen species (ROS) generation and are universally used in industrial products due to effective, eco-friendly, and low-cost advantage [19,20].

Herein, for the first time, we mention the concept using interfacial electron-withdrawing modulator of 2D photonic MOF at atomic layer level for enhanced photocatalytic disinfection. Specifically, the controllable ALD-grown metal oxides (TiO2, Fe2O3, and ZnO) on 2D MOF were prepared to generate three kinds of 2D MOF-based nanocomposites. Guided by theoretical calculations and experimental results, the optimal hybrid of 2D MOF and Fe₂O₃ was selected for further study. This atomic-layer Fe₂O₃-engineered 2D MOF significantly modulated the electronic structures of 2D MOF, including band structure and density of states. The interfacial charge transfer mechanism of 2D MOF-Fe₂O₃ revealed that the heterointerface would transfer lots of electrons from 2D MOF to Fe₂O₃ under simulated solar light irradiation, where 2D MOF and Fe₂O₃ acted as electronic donator and receptor, respectively. The effective charge transfer could extend the lifetime of photogenerated charge and improve the photocatalytic performance, thus promoting light-activated rapid disinfection (antibacterial efficacy > 99.9% at 20 min). In summary, this work provided an insight into interfacial electron-withdrawing modulator of 2D photonic MOF by ALD to optimize charge transfer pathway for promoting its photocatalytic performance.

2. Experimental section

2.1. Chemicals

Zinc nitrate hexahydrate $(Zn(NO_3)_2.6~H_2O)$ was purchased from Adamas. Tetrakis(4-carboxyphenyl)porphyrin (TCPP), pyrazine, N,N-dimethylformamide (DMF), and ethanol were purchased from Aladdin. Polyvinylpyrrolidone (PVP, average mol wt 40,000) was purchased from Sigma-Aldrich.

2.2. Synthesis of 2D MOF

The 2D MOF nanosheets were synthesized using the modified method based on the previously reported literature. First, Zn(NO₃)₂.6

 $\rm H_2O$ (18 mg, 0.06 mmol), pyrazine (3.2 mg, 0.04 mmol), PVP (80 mg), and TCPP (16 mg, 0.02 mmol) were separately added in the mixed solvent of DMF and ethanol (v/v, 3:1, 64 mL). After complete dissolution under stirring, the four solutions were mixed together and poured into Teflon-lined stainless steel autoclave. The autoclave was kept at 80 °C for 24 h, and then cooled down naturally to room temperature. To reduce the size of 2D MOF-Fe₂O₃ nanosheets, the probe sonication was used for 30 min at power density of 130 W. The resulting product were washed with ethanol and centrifuged at 10,000 r.p.m. for 15 min five times. The collected 2D MOF nanosheets were dried in 60 °C under vacuum.

2.3. Preparation of 2D MOF-TiO2, 2D MOF-Fe2O3, and 2D MOF-ZnO

The in-situ deposition of TiO_2 , Fe_2O_3 , and ZnO on 2D MOF nanosheets was achieved by atomic layer deposition (ALD, MNT-P-100–43, Micro and Nanotech Co., LTD, Wuxi, China). Each cycle was accomplished by one alternate deposition of metal and oxygen precursors, which consisted of three steps (pulse, purge, and wait) with high purity N_2 .

Atomic-layer TiO_2 deposition was performed by using tetrakis (dimethylamino)titanium (TDMAT) as titanium precursor and H_2O as oxygen precursor, respectively. The temperature of titanium and oxygen precursors was kept at 70 °C and 25 °C, respectively. During deposition, the reaction temperature and base pressure was kept at 200 °C and 20 Pa, respectively. First, the pulse, purge, and wait time of titanium precursor was 0.15, 15, and 10 s, respectively. Then, the pulse, purge, and wait time of oxygen precursor was 0.01, 20, and 10 s, respectively. The reaction was repeated 20 cycles to obtain 2D MOF-TiO₂.

Atomic-layer Fe $_2$ O $_3$ deposition was achieved by using iron tertbutoxide (ITBO) as iron precursor and H $_2$ O as oxygen precursor, respectively. The iron and oxygen precursors were maintained at 125 °C and 25 °C, respectively. During deposition, the reaction temperature and base pressure was kept at 180 °C and 20 Pa, respectively. First, the pulse, purge, and wait time of input ITBO precursor were 0.01, 1, and 0 s, respectively. Then, the pulse, purge, and wait time of output ITBO precursor were 1, 20, and 10 s, respectively. Next, the pulse, purge, and wait time of oxygen precursor was 0.02, 25, and 10 s, respectively. The reaction was repeated 20 cycles to obtain 2D MOF-Fe $_2$ O $_3$.

Atomic-layer ZnO deposition was achieved by using diethylzinc (DEZ) as zinc precursor and $\rm H_2O$ as oxygen precursor, respectively. Both of the zinc and oxygen precursors were maintained at 25 °C. During deposition, the reaction temperature and base pressure were kept at 160 °C and 20 Pa, respectively. First, the pulse, purge, and wait time of zinc precursor were 0.02, 20, and 10 s, respectively. Then, the pulse, purge, and wait time of oxygen precursor were 0.01, 25, and 10 s, respectively. The reaction was repeated 20 cycles to obtain 2D MOF-ZnO.

2.4. Morphological and componential characterization

The morphology and composition of 2D MOF, 2D MOF-TiO₂, 2D MOF-Fe₂O₃, and 2D MOF-ZnO were measured by high-resolution transmission electron microscopy (HRTEM; JEM-2100 F) equipped with energy dispersive X-ray spectroscopy (EDX). The X-ray diffraction (XRD, DX-2700BH) was used to study the crystal structure of 2D MOF, 2D MOF-TiO₂, 2D MOF-Fe₂O₃, and 2D MOF-ZnO. The Raman spectra were measured using a Raman microscope (LabRAM HR Evolution, Horiba) equipped with a 325 nm laser. The Fourier transform infrared spectrometer (FTIR, Themo Scientific) spectra were performed in the wavenumber range of 4000–450 cm $^{-1}$. The hydrodynamic size and zeta potential were detected by dynamic light scattering analysis (DLS, ZetaPALS, Brookhaven). The cumulative amounts of released ions from 2D MOF-Fe₂O₃ (200 p.p.m.) at 37 °C were appropriately diluted and detected by inductively coupled plasma atomic emission spectrometry (ICP-AES, Optimal 8000, Perkin-Elmer). The complete degradation of

2D MOF, 2D MOF-TiO $_2$, 2D MOF-Fe $_2$ O $_3$, and 2D MOF-ZnO solutions (200 p.p.m.) was achieved by adding concentrated nitric acid solution (final mass fraction was 34%) and kept at 60 $^{\circ}$ C for 12 h.

The morphology and thickness of 2D MOF and 2D MOF- Fe_2O_3 were characterized by atomic force microscopy (AFM, Bruker, Dimension icon). The X-ray photoelectron spectroscopy (XPS, Axis Supra, Kratos) was used to detect elemental composition. The cross-sectional TEM sample of 2D MOF- Fe_2O_3 nanosheets was prepared using a focused ion beam scanning electron microscope (FIB-SEM, Helios G4 PFIB). First, the 2D MOF- Fe_2O_3 nanosheets were placed on a silicon wafer. During the FIB process, the protective layers of carbon and platinum were deposited on the top of the 2D MOF- Fe_2O_3 sample, and a cross-section was cut at a 90-degree angle from the sample with a Xe ion beam. The cross-section was polished to ~ 100 nm thickness with the ion beam.

2.5. Theoretical calculation

Density-functional-theory (DFT) calculations were conducted using Cambridge Sequential Total Energy Package (CASTEP) code in Materials Studio (MS) software. Concretely, the modeling and electron-ion interaction were accomplished in accordance with plane wave basis set, ultrasoft pseudopotential, and exchange correlation potential in the generalized gradient approximation (GGA). The geometrical optimization in the Brillouin zone was based on uniform G-centered k-points meshes with $2\pi^*$ 0.03 Å⁻¹ resolution and Methfessel-Paxton electronic smearing. Moreover, the total energy was minimized by adapting cell parameters and atomic positions under the specific symmetry. All atomic forces were converged within 1 meV Å⁻¹ and total stress tensors were reduced within 0.005 GPa using finite basis-set corrections. In the electronic property calculations, one-electron valence states were expanded according to plane waves with 500 eV cutoff energy, and the corresponding parameters were modulated until sufficient convergence ($<10^{-6}$ eV). Notably, the interfacial distances between 2D MOF and metal oxides were determined by theoretical structural optimization in DFT calculations and their interfacial interactions between 2D MOF and metal oxides were van der Waals force.

2.6. Characterization of photocatalytic property

UV-vis spectrophotometer (UV-2700, Shimadzu) was employed to record UV-Vis diffuse reflectance spectra, where the film samples of 2D MOF and 2D MOF-Fe $_2$ O $_3$ on glass were prepared and used under the same condition. Photoluminescence (PL) spectrofluorometer and transient absorption (TA) spectroscopy were performed on a fluorescence spectrometer (Fluorolog-3, Horiba Jobin Yvon) with an excitation wavelength of 360 nm, where the solution samples (2D MOF, 2D MOF-TiO₂, 2D MOF-Fe₂O₃, and 2D MOF-ZnO) at same concentration (200 p.p. m.) were used. In photoelectrochemical (PEC) measurements, photocurrent response and electrochemical impedance spectroscopy (EIS) were performed on an electrochemical workstation (CHI 660E) equipped with Xenon lamp (PLS-SXE300, Beijing Perfectlight Technology Co., Ltd.) under simulated solar light irradiation at power density of 2 sun. Specifically, in a quartz glass cell in 0.5 M Na₂SO₄ aqueous solution, a three-electrode system comprised a Pt counter electrode, an Ag/AgCl reference electrode, and an experimental sample as working electrode. The film samples (2D MOF, 2D MOF-TiO2, 2D MOF-Fe2O3, and 2D MOF-ZnO) were prepared on ITO conductive glasses (1 cm \times 1 cm) under the same condition. Electron paramagnetic resonance (EPR, JES-FA200, JEOL) technique was used to examine ROS under simulated solar light irradiation at power density of 2 sun, where the spin-trap agents of 2,2,6,6-tetramethylpiperidine (TEMP, Aladdin) in water and 5,5-diemthyl-1-pyrroline N-oxide (DMPO, Sigma) in methanol were employed to trap singlet oxygen (${}^{1}O_{2}$) and superoxide anion ($\cdot O_{2}^{-}$), respectively. The solution samples (2D MOF, 2D MOF-TiO2, 2D MOF-Fe₂O₃, and 2D MOF-ZnO) at same concentration (200 p.p.m.) were used. The TiO₂ (P25, Macklin) and BiOBr (from our previous work) [21] were

chosen as photocatalytic comparison in EPR measurement.

For in-situ light-irradiated Kelvin probe force microscopy (KPFM, Bruker, Dimension icon) measurement, 2D MOF-Fe $_2O_3$ nanosheets were first placed on highly oriented pyrolytic graphite substrate to achieve high conductivity. The images were acquired at scan size of $1\times1~\mu\text{m}^2$ and the tip lift height was 80 nm at tapping mode for potential mapping, where in-situ light irradiation was performed by a Xenon lamp. Besides, in-situ XPS (Thermo escalab 250Xi) was equipped with Xenon lamp to evaluate the photocatalytic mechanism of 2D MOF and 2D MOF-Fe $_2O_3$.

2.7. In vitro antibacterial experiments

Methicillin-resistant *Staphylococcus aureus* (MRSA, ATCC 43300) and multidrug-resistant *Escherichia coli* (MDR *E. coli*, BNCC 186732) were selected and grown in standard Luria-Bertani (LB) culture medium. The antibacterial experiments were performed by spread plate method and bacterial SEM observation.

For spread plate method, the bacterial suspensions (10^7 CFU mL $^{-1}$, $200~\mu$ L) in LB culture medium were treated with PBS (control), 2D MOF (200~p.p.m.), and 2D MOF-Fe₂O₃ (200~p.p.m.) in a 96-well plate under Xenon lamp (PLS-SXE300, Beijing Perfectlight Technology Co., Ltd.) irradiation at power density of 2 sun for 20 min. Then, the treated bacterial suspensions were appropriately diluted and uniformly plated on standard LB agar plates. Next, these prepared plates were incubated at 37 °C for another 24 h to count the corresponding number of bacterial colonies by colony-forming units (CFUs). The antibacterial efficiency was calculated by the following Eq. (1), where C and E expressed the number of bacterial colonies in the control group and the experimental group (2D MOF or 2D MOF-Fe₂O₃), respectively.

Antibacterial efficiency(%) =
$$\frac{C - E}{C} * 100\%$$
 (1)

For bacterial SEM observation, the process of antibacterial procedure was consistent with that of spread plate method. After treatment, the bacteria were fixed by 2.5% glutaraldehyde (Aladdin) solution for 2 h, followed by washed with sterile PBS three times. Then, the bacteria were sequentially dehydrated by ethanol (Aladdin) solutions with different concentrations (30%, 50%, 70%, 90% and 100%, v/v) for 15 min each. Next, the treated bacteria were air-dried overnight before SEM observation.

2.8. Cutaneous MRSA wound infection model

All animal procedures and experiments of mice in this paper were approved and performed by Animal Ethical and Welfare Committee of the Institute of Radiation Medicine, Chinese Academy of Medical Sciences. C57BL/6 male mice were randomly divided into two groups: Control and 2D MOF-Fe₂O₃. First, the mice were anaesthetized by intraperitoneal injection of ketamine (100 mg kg^{-1}) and xylazine (10 mg kg^{-1}) . Next, the dorsal sides of each mouse were depilated and disinfected in order to create two symmetrical round wounds with approximately 6 mm in diameter using a biopsy punch. Then, MRSA (10⁶ CFUs) bacteria were injected into each wound to generate infected wound model. After the treatment with PBS (Control) or 2D MOF-Fe₂O₃ (0.02 mg per wound), the wounds were exposed under Xenon lamp (PLS-SXE300) irradiation at power density of 2 sun for 20 min. Afterwards, the treated wounds were covered with nonwoven fabrics and fixed with surgical adhesive. To evaluate the therapeutic effect of 2D MOF-Fe₂O₃ for MRSA-infected wounds, the wound tissues were collected and evaluated by the spread plate method on day 2. Additionally, the wounds were photographed and calculated on day 0, 2, 4, 8, and 12.

2.9. Statistical analysis

The quantitative data in this work were represented in the form of

mean values \pm standard deviations and analyzed by GraphPad Prism software. P values of *P<0.05 , **P<0.01, ***P<0.001, and ****P<0.0001 were considered statistically significant.

3. Results and discussion

3.1. Characterization of 2D MOF heterostructures

As shown in Scheme 1, three kinds of representative photocatalytic metal oxides (TiO₂, Fe₂O₃, and ZnO) were selected to modify 2D photonic MOF for engineering their interfacial electronic structures. Herein, 2D photonic MOF selected tetrakis(4-carboxyphenyl)porphyrin (TCPP) as linkers and Zn²⁺ as metal nodes. Theoretically, the self-limiting and saturated surface reactions could realize uniform atomic-layer thickness control during gas-phase deposition process of ALD system. Specifically, the in-situ growth of atomic-layer metal oxides (TiO₂, Fe₂O₃, and ZnO) on 2D MOF by ALD were accomplished by corresponding oxygen precursors (H₂O) and metal precursors, including tetrakis(dimethylamino) titanium (TDMAT), iron tert-butoxide (ITBO), and diethylzinc (DEZ). The details of experimental procedures were described in Experimental Section. The rational design of metal oxide-modified 2D MOF by ALD system aimed at optimizing its electronic structures for boosting interfacial charge transfer pathways in photocatalysis.

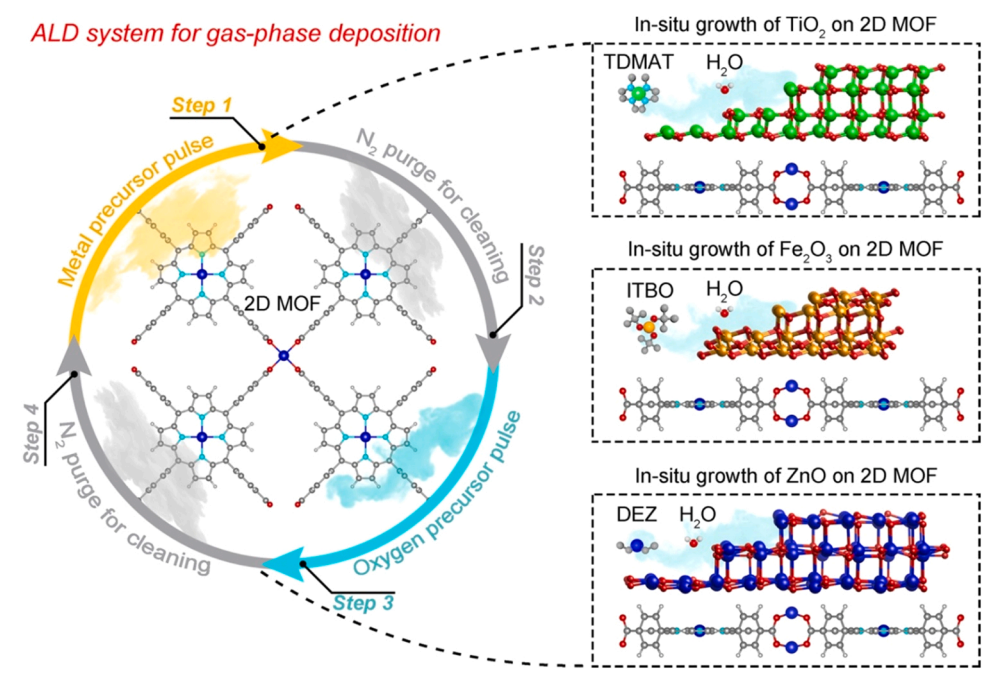
The crystal structures (Fig. 1a) of 2D MOF, 2D MOF-TiO₂, 2D MOF-Fe₂O₃, and 2D MOF-ZnO from top view were modeled by density functional theory (DFT) calculations. Notably, in the 2D MOF structure, the two kinds of active sites (ZnN₄ site and Zn₂O₈ site) were abundant, which was central to its photocatalytic mechanism. As shown in Fig. S1, the transmission electron microscopy (TEM) images and the corresponding elemental mapping images exhibited nanosheet-like morphologies and homogeneous elemental distribution of 2D MOF (Zn, C, N, and O), 2D MOF-TiO₂ (Zn, Ti C, N, and O), 2D MOF-Fe₂O₃ (Zn, Fe, C, N, and O), and 2D MOF-ZnO (Zn, C, N, and O), suggesting the uniform loading of three kinds of metal oxides on 2D MOF.

Further, as shown in Fig. S2, the elemental contents (atomic percent) of 2D MOF, 2D MOF-TiO₂, 2D MOF-Fe₂O₃, and 2D MOF-ZnO were analyzed and calculated by X-ray photoelectron spectroscopy (XPS) survey spectra (Fig. S2). The corresponding characteristic peaks in the XPS survey spectra (Fig. S2) were labelled by gray backcolor. Concretely, the 2D MOF consisted of four elements corresponding to C

1 s (77.84%), N 1 s (6.39%), O 1 s (12.20%), and Zn 2p (3.57%). Comparatively, 2D MOF-TiO₂ (C 1 s 72.05%, N 1 s 7.38%, O 1 s 15.77%, Zn 2p 3.08%, and Ti 2p 1.71%), 2D MOF-Fe₂O₃ (C 1 s 74.96%, N 1 s 6.14%, O 1 s 14.34%, Zn 2p 2.94%, and Fe 2p 1.61%), and 2D MOF-ZnO (C1 s 74.89%, N1 s 6.30%, O1 s 13.79%, and Zn 2p 5.03%) had similar C, N, and O elemental contents. Notably, the metal elements (Ti 2p 1.71% in 2D MOF-TiO₂, Fe 2p 1.61% in 2D MOF-Fe₂O₃, and Zn 2p 1.46% in 2D MOF-ZnO) indicated the similar contents of metal oxides by ALD, which was beneficial for comparison each other. However, XPS detection depth was limited by a few nanometers on sample surface. To further explore the specific ratio of each component in 2D MOF-TiO2, 2D MOF-Fe₂O₃, and 2D MOF-ZnO, the crystal structures of 2D MOF, 2D MOF-TiO₂, 2D MOF-Fe₂O₃, and 2D MOF-ZnO solution (200 p.p.m.) was completely degraded into metal ions by concentrated nitric acid solution. As shown in Fig. S3, the Zn²⁺ concentrations of 2D MOF, 2D MOF- TiO_2 , 2D MOF-Fe₂O₃, and 2D MOF-ZnO were 21.6 ± 2.0 , 18.3 ± 1.3 , 17.8 ± 0.9 , and 25.3 ± 0.8 p.p.m., respectively. the concentrations of Ti^{4+} in 2D MOF-TiO $_2$ and Fe $^{3+}$ in 2D MOF-Fe $_2\text{O}_3$ were 3.7 \pm 0.5 and 4.2 \pm 0.2 p.p.m., respectively. Therefore, the contents of metal oxides on 2D MOF were not relatively high compared with the XPS results because the number of reaction cycles of ALD-grown metal oxides on 2D MOF was only 20 cycles.

In Fig. S4, the XRD patterns of 2D MOF, 2D MOF-TiO₂, 2D MOF-Fe₂O₃, and 2D MOF-ZnO showed three typical peaks corresponding to (110), (002), and (004) of the ZnTCPP tetragonal structure of the 2D MOF [22]. Furthermore, the broad peak of (004) plane demonstrated that the ZnTCPP MOF nanosheets with ultrathin crystal nature were preferred in [001] orientation on the solid substrate. As shown in Fig. S5, the Raman spectra of 2D MOF, 2D MOF-TiO₂, 2D MOF-Fe₂O₃, and 2D MOF-ZnO included the characteristic peaks of the ZnTCPP MOF in the range of 950 - 1700 cm $^{-1}$ [9,23]. Specifically, the characteristic modes at 918, 1030, 1099, 1208, 1263, 1380, 1474, 1534, 1577, and 1633 cm $^{-1}$ were ascribed to the porphyrin core in-plane mode and phenyl ring in-plane mode of TCPP linkers in 2D MOF [9,23].

In Fig. S6, the FTIR spectra demonstrated that the peak characteristics of 2D MOF, 2D MOF-TiO₂, 2D MOF-Fe₂O₃, and 2D MOF-ZnO were mainly ascribed to those of TCPP linkers in 2D MOF [9]. Specifically, the peaks near 2950 cm $^{-1}$ were caused by C-H stretching vibrations in the aromatic ring. The peaks around 1660 and 1600 cm $^{-1}$ corresponded to the C=O and C=C stretching vibrations in the aromatic ring,



Scheme 1. Schematic illustration of ALD system for engineering 2D MOF heterojunction to screen and optimize charge transfer pathway of 2D MOF. DFT theoretical calculations are used to guide design of heterointerface. Different metal precursors (TDMAT, ITBO, and DEZ) and oxygen precursor (H₂O) are employed to deposit atomic-layer TiO₂, Fe₂O₃, and ZnO on 2D MOF, respectively. Atomic color coding in crystal structure: C-dark grey, N-cyan, O-red, H-grayish, Zn-blue, Ti-green, and Fe-deep yellow.

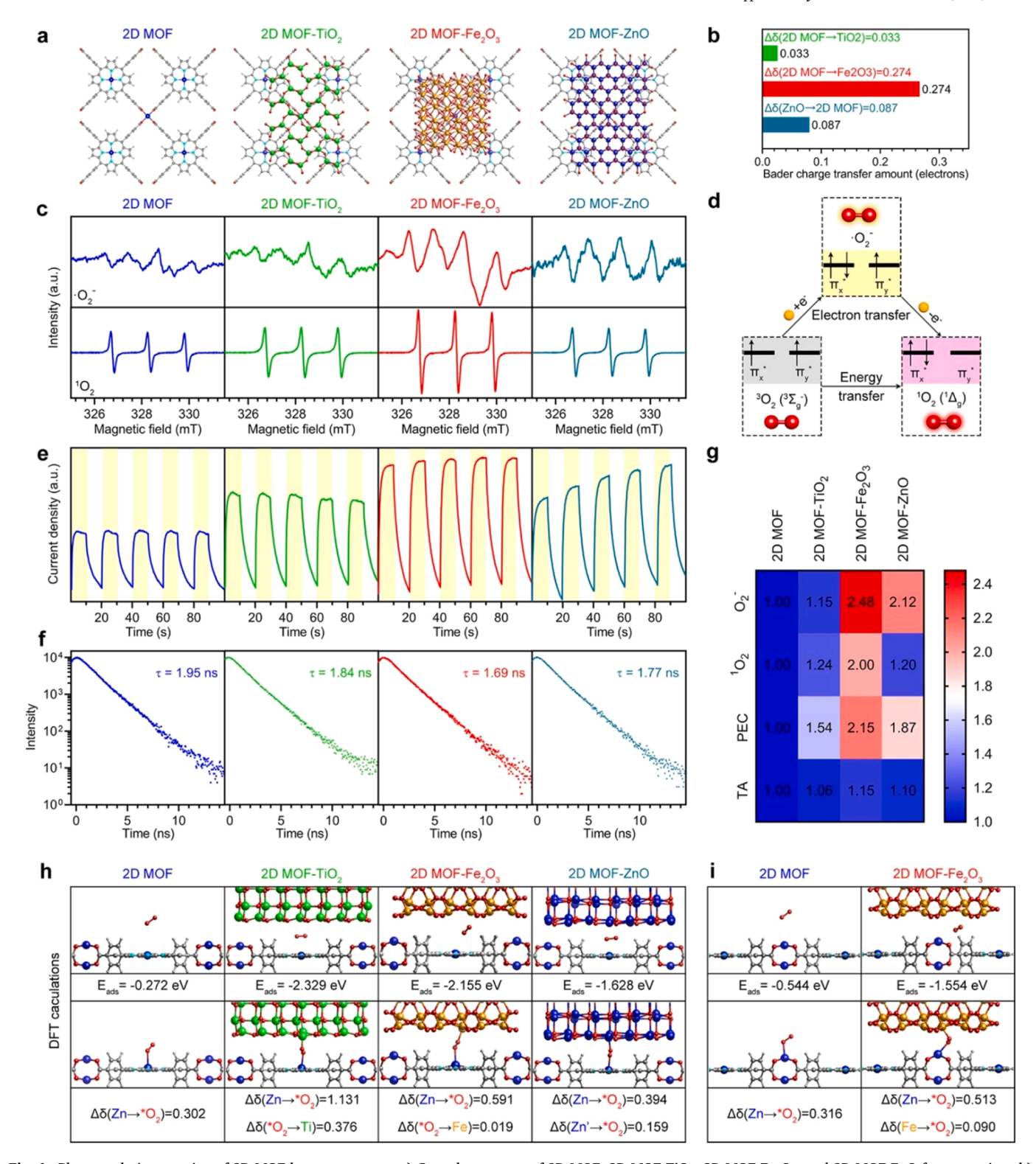


Fig. 1. Photocatalytic screening of 2D MOF heterostructures. a) Crystal structures of 2D MOF, 2D MOF-TiO $_2$, 2D MOF-Te $_2$ O $_3$, and 2D MOF-ZnO from top view. b) Bader charge calculations of 2D MOF-TiO $_2$, 2D MOF-Fe $_2$ O $_3$, and 2D MOF-ZnO models. c) EPR measurements of O_2 and 1O_2 of 2D MOF, 2D MOF-TiO $_2$, 2D MOF-Fe $_2$ O $_3$, and 2D MOF-ZnO, respectively. d) Scheme of electron spins and mutual transformation of ground triplet state ($^3\Sigma_g^-$) of 3O_2 , superoxide radical ($^3\Sigma_g^-$) and excited singlet state ($^1\Delta_g$) of 1O_2 . e) Photocurrent response curves (in the absence and presence of solar light) of 2D MOF, 2D MOF-TiO $_2$, 2D MOF-Fe $_2$ O $_3$, and 2D MOF-ZnO. f) TA spectra of 2D MOF, 2D MOF-TiO $_2$, 2D MOF-Fe $_2$ O $_3$, and 2D MOF-ZnO. g) Heatmap of screening and comparison of photocatalytic performances of 2D MOF heterostructures (2D MOF-TiO $_2$, 2D MOF-Fe $_2$ O $_3$, and 2D MOF-ZnO) relative to 2D MOF. h) DFT calculations of O_2 adsorption energy and Bader charge of adsorbed O_2 on ZnN $_4$ sites in 2D MOF, 2D MOF-TiO $_2$, 2D MOF-Fe $_2$ O $_3$, and 2D MOF-ZnO models, respectively. i) DFT calculations of O_2 adsorption energy and Bader charge of adsorbed O_2 on Zn $_2$ O $_3$ sites in 2D MOF and 2D MOF-Fe $_2$ O $_3$ models, respectively. Atomic color coding in crystal structure: C-dark grey, N-cyan, O-red, H-grayish, Zn-blue, Ti-green, and Fe-deep yellow.

respectively. The peaks at 1400 and 1000 cm $^{-1}$ were ascribed to C–H and C–O stretching vibrations, respectively. As shown in Fig. S7, the hydrodynamic average sizes of 2D MOF-TiO $_2$ (648.9 nm), 2D MOF-Fe $_2$ O $_3$ (772.9 nm), and 2D MOF-ZnO (532.4 nm) were larger than that of 2D MOF (492.0 nm), which were measured by dynamic light scattering (DLS). Additionally, the zeta potential measurements in Fig. S8 exhibited that 2D MOF (-20.7 ± 1.0 mV), 2D MOF-TiO $_2$ (-20.7 ± 0.3 mV), 2D MOF-Fe $_2$ O $_3$ (-17.2 ± 0.7 mV), and 2D MOF-ZnO (-18.6 ± 0.8 mV) were negatively charged.

The Bader charge calculations of 2D MOF-TiO $_2$, 2D MOF-Fe $_2$ O $_3$, and 2D MOF-ZnO models were shown in Fig. 1b and Table S1-S5. The electron transfer amount (0.274 electron charge from 2D MOF to Fe $_2$ O $_3$ in Table S4) in the 2D MOF-Fe $_2$ O $_3$ model was significantly more than those (0.033 electron charge from 2D MOF to TiO $_2$ in Table S3; 0.087 electron charge from ZnO to 2D MOF in Table S5) in the 2D MOF-TiO $_2$ and 2D MOF-ZnO models. Therefore, in these 2D MOF heterostrctures, TiO $_2$, Fe $_2$ O $_3$, and ZnO had negligible interactional, electron-withdrawing, and electron-donating ability, respectively. Overall, these DFT theoretical calculations provided the guidance of the material design of engineered 2D MOF heterointerfaces based on their interfacial electronic interaction. The efficient interfacial electron transfer and charge separation was beneficial for inhibiting the rapid recombination of electron-hole pairs and improving the solar-light photocatalytic activity.

3.2. Photocatalytic screening of 2D MOF heterostructures

The photocatalytic reactions to generate ROS were measured by electron paramagnetic resonance (EPR). As shown in Fig. 1c, the relative intensities of EPR characteristic peaks of superoxide radical (·O₂) and singlet oxygen (¹O₂) reflected the relative ROS yields in 2D MOF, 2D MOF-TiO2, 2D MOF-Fe2O3, and 2D MOF-ZnO groups under the same conditions (including sample concentration, light intensity, and light time). Comparatively, the 2D MOF-Fe₂O₃ group had the highest ROS (¹O₂ and·O₂) yields under simulated solar light illumination, preliminarily suggesting that the 2D MOF-Fe₂O₃ had the optimal photocatalytic activity. In Fig. S9, the photocatalytic performance for ROS (1O2) and O2) generation of 2D MOF-Fe2O3 were further compared with typical semiconductors, including TiO2 and BiOBr. Obviously, the 2D MOF-Fe $_2$ O $_3$ exhibited the highest ROS (1 O $_2$ and \cdot O $_2^-$) yields under same condition, suggesting that the ¹O₂ and ·O₂ quantum yields of 2D MOF-Fe₂O₃ were higher than TiO₂ and BiOBr. Therefore, 2D MOF-Fe₂O₃ had excellent photocatalytic ROS-generation capacity.

Besides, the electron spins and mutual transformation of ground triplet state (${}^{3}\Sigma_{g}^{-}$) of ${}^{3}O_{2}$, superoxide state of ${}^{3}O_{2}$, and excited singlet state $(^{1}\Delta_{g})$ of $^{1}O_{2}$ were schematically illustrated in Fig. 1d. Concretely, at the highest occupied molecular orbital (HOMO), the electron spins of the ground triplet state ($^3\Sigma_g^-$) of 3O_2 and the excited singlet state ($^1\Delta_g$) of 1O_2 included two unpaired electrons on individual antibonding π orbitals (π_x * and π_v *) and paired electrons on an antibonding π orbital (π_x *), respectively. Moreover, O_2 could be generated by the reduction of 3O_2 by filling an electron into π * orbital, whereas ${}^{1}O_{2}$ could be formed by the oxidation of O_2 by losing an electron in π * orbital. Overall, the direct and indirect transformations from ³O₂ to ¹O₂ could be achieved by energy transfer and electron transfer, respectively. Correspondingly, the direct photocatalytic conversion from ground ³O₂ to reactive ¹O₂ generally involved energy transfer from the excited state of photosensitizers to ground ³O₂ upon light irradiation. Besides, the electron transfer pathways in photocatalytic reactions were conducive to the formation of \cdot O₂ and ¹O₂.

As shown in Fig. 1e, the transient photocurrent response by PEC measurement exhibited that the photocurrent signal densities with five repeated on/off cycles in the presence/absence of xenon lamp irradiation in descending order were 2D MOF-Fe₂O₃, 2D MOF-ZnO, 2D MOF-TiO₂, and 2D MOF. The results preliminarily verified the more efficient charge transfer in the 2D MOF-Fe₂O₃ heterointerface under simulated

solar light irradiation. Besides, the transient photocurrent densities of 2D MOF-ZnO increased over time, which was ascribed to the relatively poor stability of 2D MOF-ZnO. In Fig. 1 f, the transient absorption (TA) spectra with 610 nm excitation indicated that the fluorescence lifetimes of 2D MOF-Fe₂O₃ (1.69 ns), 2D MOF-ZnO (1.77 ns), and 2D MOF-TiO₂ (1.84 ns) were shorter than that of 2D MOF (1.95 ns). Notably, the shorter fluorescence lifetimes of the ALD-modified 2D MOFs reflected the higher charge separation efficiency. Especially, the shortest fluorescence lifetime of 2D MOF-Fe₂O₃ suggested that the trapping of photogenerated carriers in specific sites of 2D MOF-Fe₂O₃ resulted in fastest fluorescence decay.

In Fig. 1 g, the quantitative evaluation of photocatalytic performances of 2D MOF-TiO $_2$, 2D MOF-Fe $_2O_3$, and 2D MOF-ZnO was comprehensively represented as heatmap when compared with 2D MOF. Obviously, 2D MOF-Fe $_2O_3$ exhibited the optimal photocatalytic performances by comparison of ROS (\cdot O $_2$ and 1 O $_2$) yields, PEC measurements, and TA measurements. The highest ROS yield of 2D MOF-Fe $_2$ O $_3$ heterojunctions benefited from more photo-generated holes and electrons through effective interfacial charge transfer. Theoretically, compared with the wide bandgap (\sim 3.2 eV) of TiO $_2$ and ZnO, the appropriate bandgap (\sim 2.2 eV) of Fe $_2$ O $_3$ had more efficient visible-light-responsive ability. To sum up, these experimental results collectively revealed that 2D MOF-Fe $_2$ O $_3$ heterostructure was the most efficient solar light-responsive photocatalyst. Moreover, the high ROS production of 2D MOF-Fe $_2$ O $_3$ was central to achieving the effective photocatalytic disinfection.

In order to further explore the process of energy transfer and charge transfer, the corresponding theoretical calculations based on DFT were performed. The configurations of before and after O2 adsorption in different models were shown in Fig. 1 h and the calculations of O₂ adsorption energy and Bader charge were based on the structure models after O_2 adsorption. The O_2 adsorption energies (E_{ads}) of ZnN_4 sites in 2D MOF-TiO₂ (-2.329 eV), 2D MOF-Fe₂O₃ (-2.155 eV), and 2D MOF-ZnO (-1.628 eV) models were significantly lower than that in 2D MOF (-0.272 eV) model, demonstrating that free O2 was more easily adsorbed on 2D MOF heterointerfaces. These spontaneous chemisorption processes without energy barriers (adsorption energies were less than zero) favored subsequent catalytic conversion. Similarly, in Fig. 1i, the O2 adsorption energy of Zn2O8 sites in 2D MOF-Fe2O3 (-1.554 eV) model was significantly lower than that in 2D MOF (-0.544 eV) model. Moreover, in the 2D MOF-Fe₂O₃ model, the corresponding O₂ adsorption energy in ZnN₄ site was significantly lower than that in Zn₂O₈ sites, suggesting that ZnN₄ site was more key factor affecting catalytic performance of 2D MOF-Fe₂O₃. Notably, according to the DFT calculation, the Zn₂O₈ sites in 2D MOF-TiO₂ and 2D MOF-ZnO models cannot adsorb O2 owing to their small space in Zn2O8 sites in their heterointerfaces. Among the three heterostructures, although the O2 adsorption energy of 2D MOF-Fe₂O₃ in ZnN₄ site was not the lowest, 2D MOF-Fe₂O₃ possessed two catalytic active sites (ZnN₄ site and Zn₂O₈ site). Therefore, 2D MOF- Fe_2O_3 had the huge advantage in O_2 adsorption (* O_2) and corresponding energy transfer.

Further, during the chemisorption of *O_2 , the Bader charge calculations demonstrated the significant electron transfer between adsorption sites and adsorbed *O_2 in different models due to the forming of Zn- *O (adatom) bonding, Ti- *O (adatom) bonding, and Fe- *O (adatom) bonding. Specifically, in the 2D MOF model, the electron transfer amount in the ZnN₄ site (0.302 electron charge from the Zn atom to *O_2 adatoms) was slightly less than that in the Zn₂O₈ site (0.316 electron charge from the Zn atom to *O_2 adatoms). Similarly, in the 2D MOF-Fe₂O₃ model, the net electron transfer amount of *O_2 adatoms (0.572 electron charge) in the ZnN₄ site (0.591 electron charge from the Zn atom to *O_2 adatoms; 0.019 electron charge from *O_2 adatoms to the Fe atom) was less than of that (0.603 electron charge) in the Zn₂O₈ site (0.513 electron charge from the Zn atom to *O_2 adatoms; 0.090 electron charge from the Fe atom to *O_2 adatoms). Obviously, in the ZnN₄ and Zn₂O₈ sites, the electron amounts of charge transfer from the Zn atom to

 *O_2 adatoms were significantly more than those from the Fe atom to *O_2 adatoms, suggesting that the active centers in 2D MOF were more important than those in Fe₂O₃ in the 2D MOF-Fe₂O₃ model for ROS generation, not only the interfacial electronic interaction. Besides, in the 2D MOF-TiO₂ model, the net electron transfer amount of *O_2 adatoms in

the ZnN₄ site (1.131 electron charge from the Zn atom to *O_2 adatoms; 0.376 electron charge from *O_2 adatoms to the Ti atom) was 0.755 electron charge. Similarly, in the 2D MOF-ZnO model, the net electron transfer amount of *O_2 adatoms in the ZnN₄ site (0.394 electron charge from the Zn atom in 2D MOF to *O_2 adatoms; 0.159 electron charge from

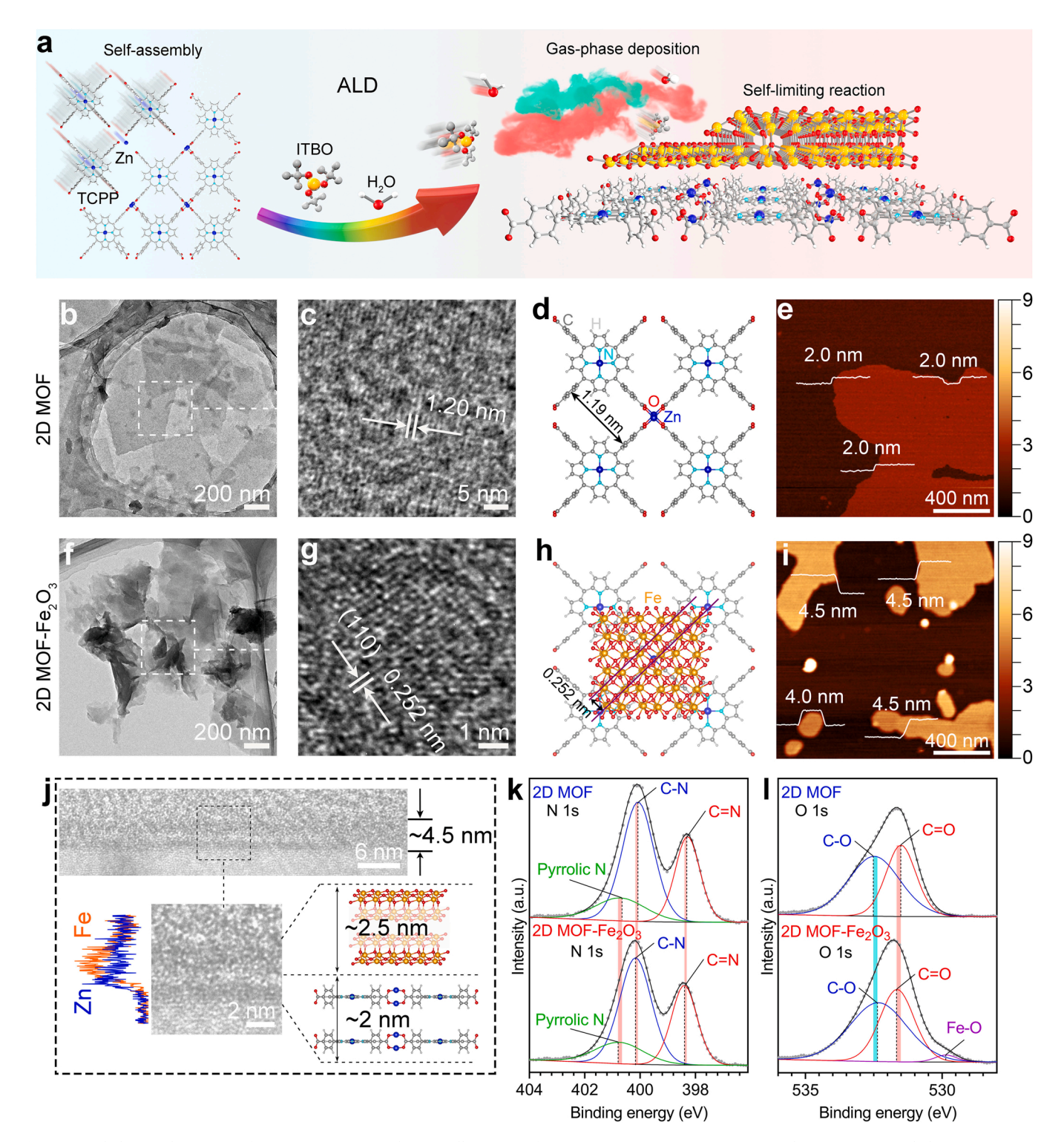


Fig. 2. Morphology and structure of 2D MOF-Fe₂O₃. (a) Schematic illustration of 2D MOF-Fe₂O₃ preparation. 2D MOF: (b) TEM image (scale bar = 200 nm), (c) corresponding HRTEM image (scale bar = 5 nm), (d) crystal structure, and (e) AFM image (scale bar = 400 nm) and corresponding height profiles. 2D MOF-Fe₂O₃; (f) TEM image (scale bar = 200 nm), (g) corresponding HRTEM image (scale bar = 1 nm), (h) crystal structure, and (i) AFM image (scale bar = 400 nm) and corresponding height profiles. (j) Cross-sectional TEM images (scale bars = 6 nm and 2 nm) of 2D MOF-Fe₂O₃, corresponding EDX spectra (Zn and Fe), and crystal structures. XPS spectra of (k) N 1 s and (l) O 1 s of 2D MOF and 2D MOF-Fe₂O₃, respectively. Atomic color coding in crystal structure: C-dark grey, N-cyan, O-red, H-grayish, Zn-blue, and Fe-deep yellow.

the Zn atom in ZnO to *O_2 adatoms) was 0.553 electron charge. Overall, the most charge transfer amounts between adsorption sites in the 2D MOF-Fe₂O₃ model and adsorbed *O_2 indicated the great advantage of 2D MOF-Fe₂O₃ heterointerface owing to the existence of two active sites (ZnN₄ site in Fig. 1 h and Zn₂O₈ site in Fig. 1i).

The adsorption energy evolution and charge transfer pathway reflected the processes of energy transfer and charge transfer, respectively. These atomistic-level mechanisms provided an insight into molecular oxygen activation of photocatalytic activity. Namely, exogenous light-activated 2D MOF and 2D MOF heterointerfaces could transfer their excited-state energy and electron charge to adsorbed ground-state *O_2 for ROS (1O_2 and 1O_2) generation. Especially, the effective interfacial charge transfer and separation of photogenerated electron-hole pairs in 2D MOF-Fe₂O₃ highlighted its potential applications in solar light-driven photocatalyst. Therefore, 2D MOF-Fe₂O₃ was selected for subsequent study about interfacial electronic engineering of 2D photonic MOF. The in-depth photocatalytic mechanism would be discussed below.

3.3. Morphology and structure of 2D MOF-Fe₂O₃

As schematically illustrated in Fig. 2a, the 2D MOF-Fe₂O₃ nanosheets were prepared by two steps. First, 2D MOF nanosheets were formed by the self-assembly of TCPP and Zn²⁺ by a solvothermal method. Then, the ultrathin 2D MOF nanosheets were exfoliated by probe sonication. Further, the atomic-layer Fe₂O₃-modified 2D MOF nanosheets by gasphase deposition were accurately achieved by self-limiting reaction of ITBO and H₂O in ALD system. The 2D MOF nanosheets observed by TEM (Fig. 2b) had uniform lamellar structure. The corresponding highresolution TEM (HRTEM) image (Fig. 2c) of 2D MOF displayed a lattice fringe with interplanar distance of 1.20 nm, which could be in accordance with the theoretical interplanar distance of 1.19 nm based on the simulated crystallographic structure (Fig. 2d). Besides, as shown in Fig. 2e, the AFM image and the corresponding height profiles of 2D MOF demonstrated the average thickness of ~2.0 nm, which nearly approached the two-layer thickness of MOF nanosheets [22]. The obtained ultrathin structure with relatively high specific surface area was conducive to exposing more catalytic active sites (ZnN₄ and Zn₂O₈ sites).

Comparatively, the 2D MOF-Fe₂O₃ nanosheets (TEM image in Fig. 2f) showed visually thicker lamellar morphology. As mentioned above, the element mappings of TEM image (Fig. S1) of the 2D MOF-Fe₂O₃ nanosheet exhibited the homogeneous distribution of individual elements of Zn, Fe, C, N, and O, suggesting the uniform loading of Fe₂O₃ on 2D MOF. The HRTEM image (Fig. 2g) of the 2D MOF-Fe₂O₃ demonstrated an interplanar distance of 0.252 nm corresponding to (110) lattice plane of hematite (α-Fe₂O₃). The theoretical crystal structure (Fig. 2h) of 2D MOF-Fe₂O₃ also marked a lattice distance of 0.252 nm, which could be consistent with the experimental result. As shown in Fig. 2i, the AFM image and the corresponding height profiles exhibited that the average thickness of 2D MOF-Fe₂O₃ (~4.3 nm) was \sim 2.3 nm thicker than that of 2D MOF (\sim 2.0 nm). To sum up, the atomic layer deposition (ALD) of Fe₂O₃ could obtain uniform 2D MOF-Fe₂O₃ heterostructure. In Fig. 2j, the cross-sectional TEM images of 2D MOF-Fe₂O₃ also indicated a uniform thickness (~4.5 nm), where the thicknesses of 2D MOF and Fe₂O₃ were \sim 2 nm and \sim 2.5 nm, respectively. The Zn and Fe signals detected by the corresponding EDX spectra demonstrated the chemical composition of 2D MOF and Fe₂O₃ nanolayers, respectively. Moreover, the corresponding crystal structure was schematically illustrated. Additionally, the metal ion leaching curves of 2D MOF-Fe₂O₃ (200 p.p.m.) for long-term release (14 days) were shown in Fig. S10. Over time, the cumulative Zn^{2+} (1.92 \pm 0.14 p.p.m.) and $\mathrm{Fe^{3+}}$ (0.33 \pm 0.02 p.p.m.) release within 14 days was stable and slow, which were obviously lower than those of total degradation (Fig. S3). The low degree of metal ion leaching demonstrated that 2D MOF-Fe₂O₃ in water for 14 days had slight degradation and relative stability.

To further confirm the existence of interfacial interaction between

2D MOF and Fe₂O₃, the XPS elemental spectra (Fig. 2k, l, and Fig. S11) of the 2D MOF and 2D MOF-Fe₂O₃ nanosheets were systematically compared. In Fig. S11a, the C1 s signals of 2D MOF and 2D MOF-Fe₂O₃ were calibrated to 284.8 eV and divided into C=C (284.8 eV), C-C/C-H (286.2 eV), C-N/C-O (288.2 eV), and C=N/C=O (290.7 eV for 2D MOF and 290.5 eV for 2D MOF-Fe₂O₃) [24]. In Fig. 2k, the N 1 s peak of 2D MOF was ascribed to three subpeaks corresponding to C=N (398.3 eV), C-N (400.0 eV), and pyrrolic N (400.5 eV) groups [24,25]. Comparatively, the three subpeaks of C=N (398.4 eV), C-N (400.2 eV), and pyrrolic N (400.8 eV) groups of 2D MOF-Fe₂O₃ shifted to higher binding energy. Besides, the O 1 s regions (Fig. 21) comprised C=O (531.5 eV for 2D MOF and 531.7 eV for 2D MOF-Fe₂O₃) and C-O (532.5 eV for 2D MOF and 532.3 eV for 2D MOF-Fe₂O₃) groups. Simultaneously, the O 1 s region of the 2D MOF-Fe₂O₃ contained Fe-O (529.9 eV) group [24,26]. Obviously, the peaks of C=O and C-O groups of 2D MOF-Fe₂O₃ had higher and lower binding energy than those of 2D MOF, respectively. Notably, the peak shift of five groups confirmed that 2D MOF-Fe₂O₃ heterointerface had certain interfacial interaction. Besides, the Zn 2p peaks of 2D MOF and 2D MOF-Fe₂O₃ were shown in Fig. S11b. The Fe 2p peak (Fig. S11c) of 2D MOF-Fe₂O₃ was assigned to Fe $2p_{3/2}$ (711.1 and 724.0 eV), Fe $2p_{1/2}$ (714.8 and 727.4 eV), and satellite (717.6 eV), which was in good agreement with that of hematite (α-Fe₂O₃) in previous literature [27]. Additionally, ALD-grown wurtzite ZnO structure had been confirmed in our previous work [28]. ALD-grown rutile TiO2 structure was studied in previous literature [29]. The crystal structure of the 2D MOF-Fe₂O₃ heterointerface was illustrated in Fig. S11d.

3.4. Photocatalytic mechanism

As depicted in Fig. 3a, the UV-Vis diffuse reflectance spectra indicated that the absorbance characteristics of 2D MOF and 2D MOF-Fe₂O₃ included a strong Soret band (marked by light blue backcolor, 350-400 nm) and three Q bands (marked by pink backcolor, 400-660 nm) in UV-Vis range (250-850 nm). This optical feature was ascribed to the photophysical properties of porphyrinic structure from MOF linkers (TCPP) [30]. Notably, 2D MOF-Fe₂O₃ had the higher absorbance than 2D MOF and the corresponding four absorbance peaks of 2D MOF-Fe₂O₃ had an obvious redshift (the details were shown in Fig. S12) compared with 2D MOF. The high and red-shift absorbance of 2D MOF-Fe₂O₃ demonstrated that the interaction between 2D MOF and Fe₂O₃ was beneficial for improving the optical behavior of 2D MOF. Besides, the band structures of 2D MOF and 2D MOF-Fe₂O₃ were important to understanding the mechanism of photocatalysis. In Fig. 3b, according to the calculation based on Kubelka-Munk function versus bandgap energy, 2D MOF had a bandgap of 1.84 eV [31].

In Fig. 3c, the photoluminescence (PL) spectra of 2D MOF and 2D MOF-Fe₂O₃ exhibited similar curve shapes with two obvious peaks corresponding to \sim 620 and \sim 660 nm. The PL signal intensity of 2D MOF-Fe₂O₃ was weaker than that of 2D MOF and the peak position near 620 nm had a redshift of \sim 8 nm. The strong PL intensity of 2D MOF demonstrated a relatively rapid charge recombination rate, while the weaker PL intensity of 2D MOF-Fe₂O₃ revealed an effective reduction of recombination of photo-generated electron-hole pairs. Namely, the 2D MOF-Fe₂O₃ heterojunction could efficiently separate photo-excited electron-hole pairs into 2D MOF and Fe₂O₃ across the heterointerface, causing prolonged charge carrier lifetime and enhanced photocatalytic activity. Additionally, the redshifted peak of 2D MOF-Fe₂O₃ illustrated a hybridization of electronic states between 2D MOF and Fe₂O₃ [32].

As shown in Fig. 3d, the electrochemical impedance spectroscopy (EIS) measurements in the presence and absence of simulated solar light irradiation revealed that the smaller semicircle arc of 2D MOF-Fe₂O₃ represented the lower internal resistance and faster interfacial electron transfer than that of 2D MOF. Consequently, the PEC studies (Figs. 1e and 3d) concluded that 2D MOF-Fe₂O₃ improves the mobility of the photo-induced charges between 2D MOF and Fe₂O₃, preventing

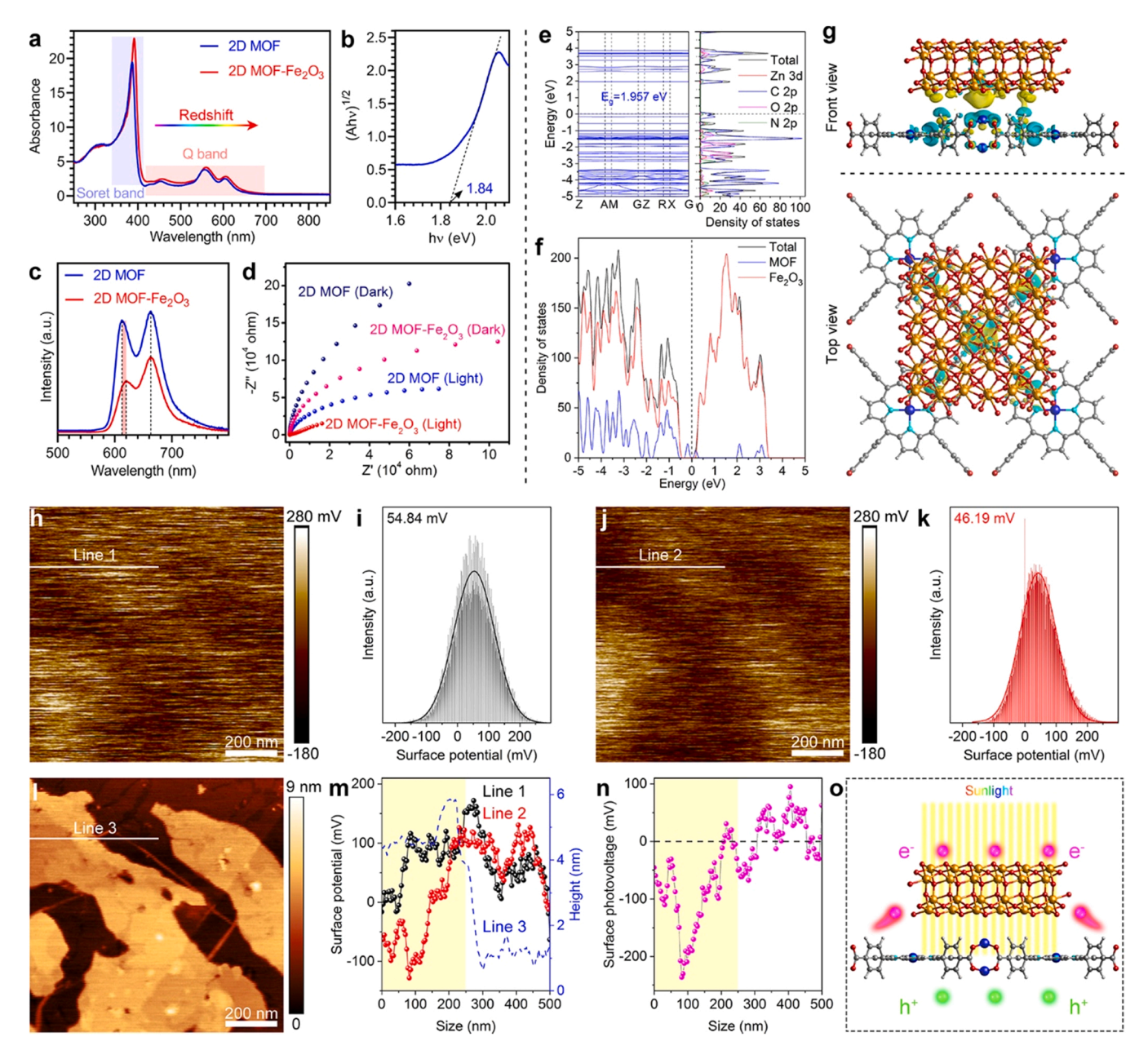


Fig. 3. Photocatalytic mechanism. (a) UV-Vis diffuse reflectance spectra of 2D MOF and 2D MOF-Fe₂O₃, (b) Plots of $(\alpha h \nu)^{1/2}$ versus photon energy $(h\nu)$ of 2D MOF, and (c) PL spectra of 2D MOF and 2D MOF-Fe₂O₃, (d) EIS curves of 2D MOF and 2D MOF-Fe₂O₃ in the absence and presence of solar light. (e) DFT theoretical calculations of band structure and corresponding DOS of 2D MOF. (f) DFT calculations of 2D MOF-Fe₂O₃ model of total DOS and project DOS of 2D MOF and Fe₂O₃, (g) 3D charge density difference plot of 2D MOF-Fe₂O₃ heterointerface from front view and top view, respectively. Fermi level is defined as zero. Atomic color coding in crystal structure: C-dark grey, N-cyan, O-red, H-grayish, Zn-blue, and Fe-deep yellow. Charge distribution of cyan and yellow regions corresponding to charge density depletion and accumulation, respectively. (h) KPFM image and (i) corresponding surface potential distribution of 2D MOF-Fe₂O₃ in dark. (j) KPFM image and (k) corresponding surface potential distribution of 2D MOF-Fe₂O₃ upon solar light illumination. (l) Corresponding AFM topography image of 2D MOF-Fe₂O₃ (scale bars = 200 nm for all images). (m) Surface potential and height profiles locating at same position corresponding to Line 1–3 (Region marked by yellow backcolor represented 2D MOF-Fe₂O₃ surface). (n) Surface photovoltage profile by subtracting the surface potentials under dark and light irradiation conditions. (o) Schematic illustration of photogenerated electron–hole separation and distribution on 2D MOF-Fe₂O₃ surface.

photogenerated electron-hole pair recombination under solar light irradiation.

As shown in Fig. 3e, the band structure and density of states (DOS) of 2D MOF were calculated according to DFT, where the highest occupied orbital was set as a reference (0 eV) and chosen as the Fermi energy level. Obviously, the band structure of the 2D MOF indicated that the 2D MOF possessed a typical characteristic of semiconductor with an appropriate bandgap (1.957 eV). For the DOS curves of 2D MOF (Fig. 3e), the area near highest occupied molecular orbital (HOMO) predominantly consisted of C 2p and N 2p states. Meanwhile, the area

near lowest unoccupied molecular orbital (LUMO) mainly comprised C 2p and N 2p states, hybridized with some Zn 3d state. The curves in Fig. 3e were enlarged in Fig. S13a to clearly show the curves of different elements. In Fig. S13b, the band structure of Fe_2O_3 also exhibited a typical semiconductor with a bandgap of 1.824 eV. The corresponding valence band maximum (VBM) and conduction band minimum (CBM) were located at the G point and K point in the Brillouin zone, respectively. Moreover, the region near VBM of Fe_2O_3 mainly consisted of O 2p states including hybridization with few Fe 3d states, whereas the zone near CBM was occupied by Fe 3d states slightly hybridized with O 2p

states.

As depicted in Fig. 3f, the total DOS of 2D MOF-Fe $_2O_3$ and the corresponding projected DOS of 2D MOF and Fe $_2O_3$ demonstrated their electronic coupling and orbital contributions in heterostructure. Concretely, the zones near HOMO and LUMO of 2D MOF-Fe $_2O_3$ heterostructure primarily originated from 2D MOF and Fe $_2O_3$, respectively.

Notably, the electronic DOS of 2D MOF- Fe_2O_3 provided detailed component contributions to energy levels to predict the locality and direction of electron transfer.

As shown in Fig. 3g, the 3D charge density difference plot based on the optimized structure of 2D MOF-Fe₂O₃ was calculated to investigate the charge distribution along the heterointerface. Obviously, a large

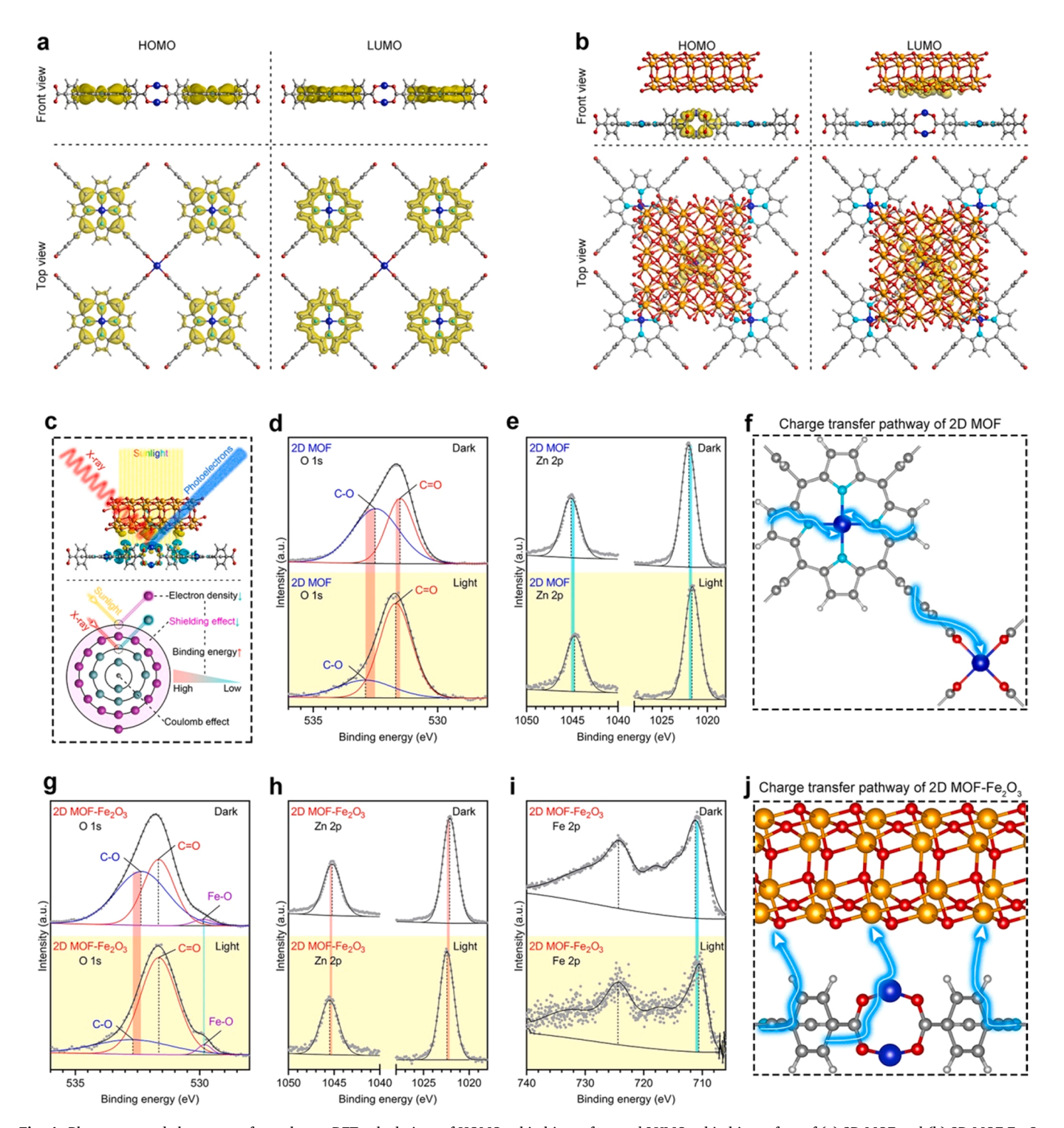


Fig. 4. Photogenerated charge transfer pathway. DFT calculations of HOMO orbital isosurface and LUMO orbital isosurface of (a) 2D MOF and (b) 2D MOF- Fe_2O_3 from front view and top view, respectively. (c) Schematic diagram of ISI-XPS device for analyzing 2D MOF- Fe_2O_3 heterointerface under solar light, and schematic illustration of shielding effect of outer electrons and Coulomb effect of nucleus to affect binding energy of inner electrons. ISI-XPS spectra of (d) O 1 s and (e) Zn 2p of 2D MOF before and after illumination, respectively. (f) Charge transfer pathway of 2D MOF. ISI-XPS spectra of (g) O 1 s, (h) Zn 2p, and (i) Fe 2p of 2D MOF- Fe_2O_3 before and after illumination, respectively. (j) Charge transfer pathway of 2D MOF- Fe_2O_3 . Atomic color coding in crystal structure: C-dark grey, N-cyan, O-red, H-grayish, Zn-blue, and Fe-deep yellow.

amount of differential charges accumulated in the interfacial region of 2D MOF-Fe $_2$ O $_3$. Moreover, the interfacial charges had coupling interactions between 2D MOF and Fe $_2$ O $_3$ in the ground electronic state, which was beneficial for charge migration along the heterointerface. Consequently, this 2D MOF-Fe $_2$ O $_3$ heterostructure might favor the charge transfer pathway of the photogenerated electrons and inhibit the recombination rate of electron-hole pairs.

To further probe the spatial location of the photogenerated electrons and holes on 2D MOF-Fe₂O₃ surface, the in-situ light-irradiated KPFM was performed. As shown in Fig. 3h-k, the KPFM images and the corresponding surface potential distributions of 2D MOF-Fe₂O₃ had spatial variation in dark and upon solar light illumination, suggesting the spatial photogenerated charge transfer and separation at nanometer scale. The corresponding AFM topography image (Fig. 3 l) of 2D MOF- Fe_2O_3 and its height profile (Fig. 3 m, Line 3) indicated $\sim\!4.5\;\text{nm}$ thickness, which were well consistent with the above result (Fig. 2i). Concretely, the KPFM images (Fig. 3 h and 3j) visually demonstrated that the surface potential of 2D MOF-Fe₂O₃ decreased after light irradiation. Besides, the corresponding average surface potential under light irradiation (Figs. 3k, 46.19 mV) was 8.65 mV lower than that in dark (Figs. 3i, 54.84 mV). The solar light-induced surface potential decrease was attributed to the accumulation of photogenerated electrons on 2D MOF-Fe₂O₃ surface. Moreover, the corresponding cross-line profiles (Fig. 3 m) locating at same position also exhibited that the surface potential under light irradiation (Line 2) was significantly lower than that under dark (Line 1). Notably, the region of potential change mainly focused on the 2D MOF-Fe₂O₃ surface (marked by yellow backcolor in Fig. 3 m and n). Correspondingly, the surface photovoltage profile (Fig. 3 n) reflected spatial photogenerated charge distribution by subtracting the surface potential under dark from the surface potential under solar light irradiation. Obviously, the 2D MOF-Fe₂O₃ surface photovoltage was less than zero and the minimum value was less than - 200 mV, further confirming the photoelectron accumulation on 2D MOF-Fe₂O₃ surface. As schematically illustrated in Fig. 3o, the spatial charge distribution on 2D MOF-Fe₂O₃ surface demonstrated the photogenerated electron-hole separation into Fe₂O₃ and 2D MOF, respectively.

3.5. Photogenerated charge transfer pathway

To further explore the photogenerated charge transfer and separation process, the HOMO orbital isosurface and LUMO orbital isosurface of 2D MOF and 2D MOF-Fe₂O₃ were systematically calculated. In Fig. 4a, from front and top view, the charge distributions of HOMO and LUMO of 2D MOF mainly focused on the region of porphyrinic ring. Compared with that of HOMO of 2D MOF, the distribution of charge density of LUMO was more uniform, suggesting certain charge transfer among C, N, O, and Zn elements under solar light illumination. In contrast, in Fig. 4b, the charge distributions of HOMO and LUMO of 2D MOF-Fe₂O₃ mostly concentrated on 2D MOF and Fe₂O₃, respectively. Therefore, the transfer direction of photoexcited electrons was from 2D MOF side to Fe₂O₃ side across the heterointerface. Namely, the photoexcited electron-hole pairs would be well separated at different sides along the heterointerface, which efficiently prolonged the lifetime of photogenerated charges.

Experimentally, in-situ synchronous illumination X-ray photoelectron spectroscopy (ISI-XPS) was employed to comprehensively investigate the details of photogenerated charge migration in 2D MOF and 2D MOF-Fe₂O₃. The working mechanism of ISI-XPS device was schematically illustrated in Fig. 4c. Concretely, X-ray and simulated solar light (imported by Xenon lamp) were simultaneously employed to irradiate 2D MOF and 2D MOF-Fe₂O₃. The corresponding binding energies of photoelectrons were detected to analyze electronic structures and valence states under excited state. Notably, the shift of binding energy was manipulated by the change of outer electron density because the binding energy of atomic inner electrons was determined by Coulomb

effect of atomic nucleus and shielding effect of outer electrons. Namely, when Coulomb effect of atomic nucleus was constant, the increase of outer electron density would enhance its shielding effect, leading to the decrease of binding energy. Conversely, the decrease of outer electron density would weaken its shielding effect, causing the increase of binding energy.

As shown in Fig. 4d, the two characteristic peaks (C-O and C=O) of O 1 s of 2D MOF shifted to higher binding energy after light irradiation, indicating that the outer electron density of O atoms decreased under light illumination. Similarly, the higher binding energy of C 1 s (C=N/ C=O and C-N/C-O) and N 1 s (Pyrrolic N and C-N) of 2D MOF (Fig. S14) also suggested the decreased photoelectron densities of C and N atoms. In contrast, the lower binding energy of Zn 2p of 2D MOF (Fig. 4e) implied that the photogenerated electrons were transferred from C, N, and O atoms to Zn atoms. As schematically illustrated in Fig. 4 f, the possible photogenerated charge transfer pathways of 2D MOF were marked by cyan arrows, focusing on LMCT process. Specifically, in porphyrinic rings in 2D MOF, the photoelectrons locating in C=N bond and pyrrolic N sites were moved to Zn atoms in ZnN₄ sites. In metal clusters in 2D MOF, the photoelectrons locating in C-O and C=O bonds were transferred to Zn atoms in Zn₂O₈ sites. Therefore, the abundant photoelectrons in active sites (ZnN₄ and Zn₂O₈ sites) were beneficial for

In Fig. 4 g, the O 1 s peaks corresponding to C-O and Fe-O bonds in 2D MOF-Fe₂O₃ shifted to higher and lower positions, respectively. Besides, the binding energies of Zn 2p (Fig. 4 h) and Fe 2p (Fig. 4i) moved to higher and lower positions, respectively. Meanwhile, the shifted binding energy of C 1 s (C=N/C=O and C-N/C-O) and N 1 s (Pyrrolic N and C-N) of 2D MOF-Fe₂O₃ (Fig. S15) also indicated the changed photoelectron densities of C and N atoms. The possible photogenerated charge transfer pathways of 2D MOF-Fe₂O₃ (Fig. 4j, cyan arrows) centered on the heterointerface between 2D MOF and Fe₂O₃. Namely, once 2D MOF-Fe₂O₃ was irradiated by simulated solar light, the photogenerated electrons would migrate from 2D MOF to Fe₂O₃ across the heterointerface, including the pathways from Zn₂O₈ and C-O bonds to Fe-O bonds. Hence, these photogenerated charge transfer pathways detected by ISI-XPS were in good agreement with the theoretical results (Fig. 4a and b) and light-irradiated KPFM (Fig. 3h-o).

To sum up, the porphyrinic linkers (TCPP) and metal clusters (ZnN4 and Zn₂O₈ nodes) in 2D MOF acted as light harvesters and active catalytic centers, respectively. The mechanism of the photocatalytic process of 2D MOF was that the photogenerated electrons rapidly transferred from TCPP orbitals to ZnN₄ and Zn₂O₈ orbitals, improving the charge separation. In electron donor-acceptor system of 2D MOF structure, this ligand-to-metal charge transfer (LMCT) process involved partial electron transfer from ligand-localized orbitals (large π -conjugation system of TCPP) to metal-localized orbitals (ZnN₄ and Zn₂O₈ nodes) during the transition from excited states to the ground state upon light irradiation.

For each individual component, abundant photogenerated electrons of 2D MOF would be manly transported among C 2p, N 2p, and Zn 3d states under solar light irradiation, while plentiful photogenerated electrons of Fe_2O_3 will be mostly moved from O 2p to Fe 3d. Comparatively, the 2D MOF- Fe_2O_3 heterointerface served as an available electron transfer pathway. Namely, under solar light irradiation, 2D MOF- Fe_2O_3 heterointerface would transfer lots of electrons from 2D MOF to Fe_2O_3 , where 2D MOF and Fe_2O_3 acted as electronic donator and receptor, respectively. The effective charge transfer could extend the lifetime of photogenerated electron, thus promoting the photocatalytic performance.

3.6. Photocatalytic disinfection performance

As shown in Fig. 5a, the antibacterial mechanism of photocatalytic disinfection was schematically illustrated. Specifically, the 2D MOF-Fe₂O₃ heterostructure generated lots of ROS (1 O₂ and 1 O₂) under simulated solar light, achieving rapid photocatalytic antibacterial action

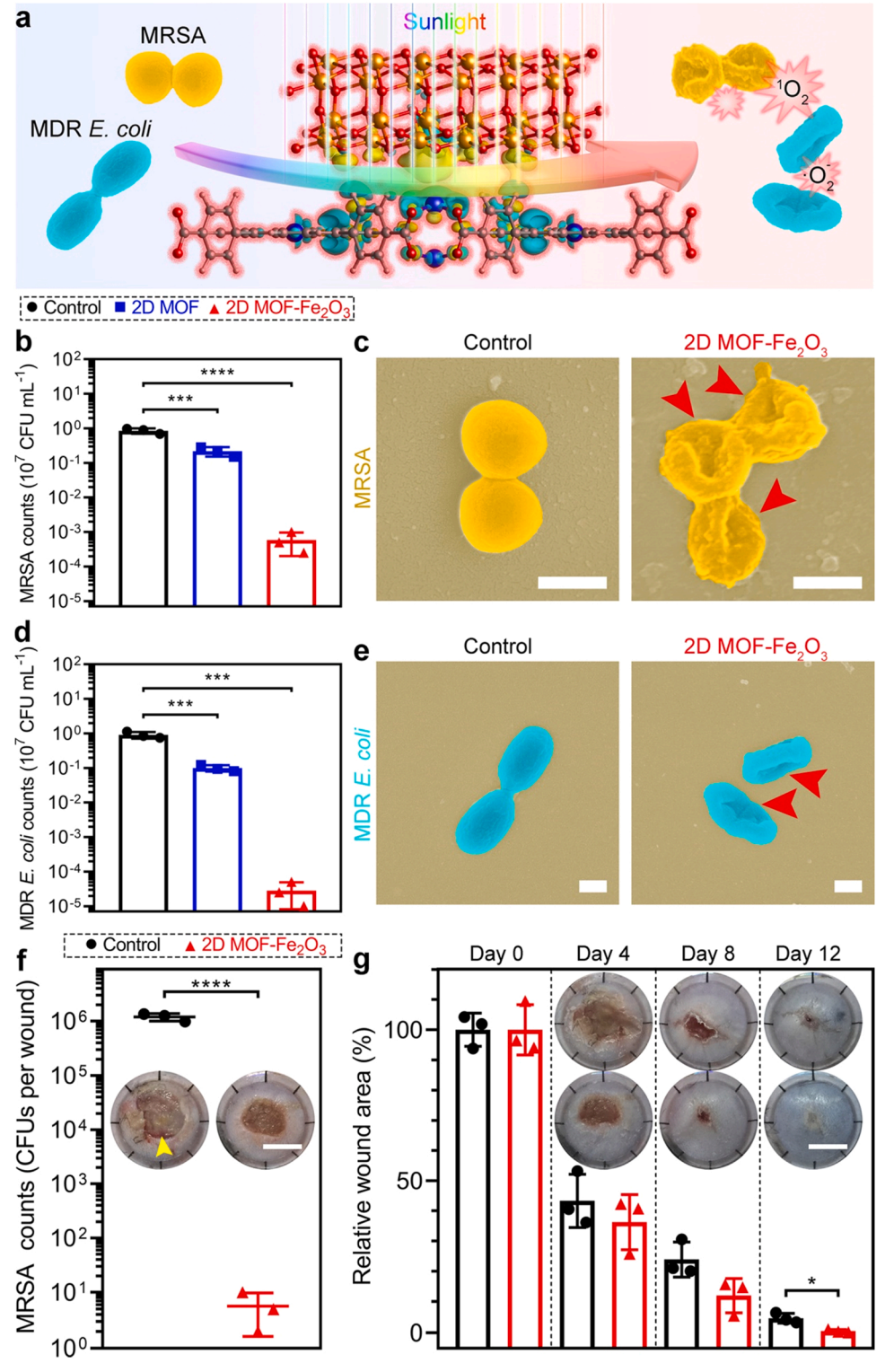


Fig. 5. Photocatalytic disinfection performance. (a) Schematic illustration of 2D MOF-Fe₂O₃ for photocatalytic antibacterial action. (b) Viabilities of MRSA treated with 2D MOF and 2D MOF-Fe₂O₃ under solar light irradiation for 20 min, respectively. (c) SEM images of MRSA treated with 2D MOF-Fe₂O₃ under solar light irradiation for 20 min (scale bars = 500 nm). (d) Viabilities of MDR E. coli treated with 2D MOF and 2D MOF-Fe₂O₃ under solar light irradiation for 20 min, respectively. (e) SEM images of MDR E. coli treated with 2D MOF-Fe₂O₃ under solar light irradiation for 20 min (scale bars = 500 nm). Red arrows in SEM images mark obvious damage and deformation of bacteria. (f) Photographs of MRSAinfected wounds on days 2 (Yellow arrows mark serious suppuration on wound, scale bars 5 mm) and corresponding quantitative assessment of MRSA counts in wounds by spread plate method. (g) Representative photographs of wound healing process over time and corresponding quantitative analysis of wounds (scale bars = 5 mm). Individual data points (n = 3 biologically independent samples) and error bars indicate means \pm standard deviations. Statistical differences were analyzed by one-way ANOVA and post hoc Tukey's test or a two-tailed Student's t-test (* P < 0.05, ** P < 0.01, *** P < 0.001, **** P < 0.0001).

against drug-resistance bacteria, including MRSA and MDR *E. coli*. As shown in Fig. S16, the photocatalytic disinfection performance of 2D MOF-Fe₂O₃ (200 p.p.m.) at different photon fluxes was investigated for 20 min. Obviously, the corresponding antibacterial rates (89.75 \pm 1.74%, 99.06 \pm 0.44%, and 99.9968 \pm 0.0007%) against MDR *E. coli* increased with increasing light power densities (0.5, 1, and 2 sun). As shown in Fig. S17, the photocatalytic disinfection performance of 2D MOF-Fe₂O₃ (200 p.p.m.) at different liquid depth (1, 3, and 5 cm) was measured for 20 min. Obviously, the corresponding antibacterial rates

(99.26 \pm 0.27%, $\,$ 99.97 \pm 0.02%, and $\,$ 99.9969 \pm 0.0011%) against MDR E. coli decreased with increasing liquid depths (1, 3, and 5 cm) under solar light irradiation (2 sun). Therefore, the optimized power density (2 sun) and liquid depth (1 cm) were selected in the following study.

In Fig. 5b, the antibacterial rate of 2D MOF-Fe₂O₃ (99.9315 \pm 0.0448%) was higher than that of 2D MOF (74.3349 \pm 7.7913%) against MRSA under simulated solar light for 20 min. The corresponding scanning electron microscope (SEM) images (Fig. 5c) exhibited that the

MRSA bacteria with broken membranes in the 2D MOF-Fe $_2$ O $_3$ group became corrugated (marked by red arrows) when compared with that of the control group. Similarly, the 2D MOF-Fe $_2$ O $_3$ group (99.9969 \pm 0.0022%) had a higher antimicrobial efficiency than the 2D MOF group (89.0562 \pm 2.2782%) against MDR *E. coli* in Fig. 5d. The corresponding morphology of MDR *E. coli* bacteria in the control group presented a rod-like shape with intact membranes, whereas the MDR *E. coli* bacteria in the 2D MOF-Fe $_2$ O $_3$ group displayed a serious deformation (marked by red arrows in Fig. 5e). In summary, the 2D MOF-Fe $_2$ O $_3$ heterojunction demonstrated a broad-spectrum antibacterial activity under simulated solar light because the rapid ROS generation could effectively destroy the bacterial membranes of different kinds of bacteria.

Further, the cutaneous MRSA wound infection model was used to evaluate the in vivo therapeutic efficacy of 2D MOF-Fe₂O₃. At 2 days post infection, the infected wound in the control group demonstrated severe suppuration (marked by yellow arrow in Fig. 5 f) due to heavy MRSA burdens in the wounds. In contrast, the infected wound in 2D MOF-Fe₂O₃ group by photocatalytic disinfection treatment indicated no obvious inflammatory response and complete escharosis. Moreover, the 2D MOF-Fe₂O₃ group exhibited excellent bacterial killing efficiency against MRSA on day 2 (99.9995 \pm 0.0003%) in vivo (Fig. 5 f), which was well consistent with the antibacterial results in vitro (Fig. 5b).

As shown in Fig. 5 g, compared with the control group, the 2D MOF-Fe₂O₃ group displayed accelerated wound closure over time. Therefore, the negligible levels of MRSA counts and the smaller wound sizes in the 2D MOF-Fe₂O₃ group fully demonstrated efficacious bacterial eradication and accelerated wound healing. In summary, the excellent performance of photocatalytic disinfection of 2D MOF-Fe₂O₃ highlighted great potential in water disinfection and wound disinfection. Notably, the summary and comparison of 2D MOF-based photocatalytic materials in recent literatures with our works were listed in Table S6 [10,33-36]. 2D MOF-based nanocomposites had great potential in photocatalytic field and the corresponding photocatalytic mechanisms included photogenerated electron transfer and active sites. Comparatively, the ALD-grown Fe₂O₃ on 2D MOF in this work had unique processing method (ALD) and photocatalytic mechanism (electron-withdrawing effect). Therefore, this multifunctional platform preliminarily exhibited a certain potential in photocatalytic applications.

4. Conclusion

In this work, atomic layer deposition (ALD)-grown metal oxides (TiO₂, Fe₂O₃, and ZnO) on 2D MOF (ZnTCPP) engineered its interfacial electronic structure to improve charge transfer and enhance photocatalysis. After screening by theoretical calculations and experimental results, the 2D MOF-Fe₂O₃ exhibited the highest ROS yield under solar light irradiation due to relatively lower absorption energy and more charge transfer amount of adsorbed *O2. Moreover, the 2D MOF-Fe2O3 heterostructure significantly regulated the band structure and density of states of 2D MOF. The interfacial charge transfer mechanism of 2D MOF-Fe₂O₃ demonstrated that the heterointerface transferred lots of photoelectrons from 2D MOF to Fe₂O₃ under solar light irradiation, where 2D MOF and Fe₂O₃ acted as electronic donator and receptor, respectively. The optimized charge transfer pathway can prolong the lifetime of photogenerated charges, thus promoting the photocatalytic disinfection performance (antibacterial efficacy > 99.9% at 20 min) against MRSA and MDR E. coli. To sum up, this platform provided an insight into interfacial electron-withdrawing modulator of 2D photonic MOFs to optimize charge transfer pathway for improving their catalytic property.

CRediT authorship contribution statement

J.L., X.L. and S.W. conceived and designed the concept of the experiments. J.L. synthesized the materials and conducted the material characterizations. J.L., X.L. and S.W. analysed the experimental data

and co-wrote the manuscript. **Z.C.**, **Y.Z.**, **H.J.**, **Z.L.**, **S.Z.**, **Y.Z.**, **and P.C.** provided important experimental insights. All the authors discussed, commented and agree on the manuscript.

Declaration of Competing Interest

The authors declare that they have no known competing financial interests or personal relationships that could have appeared to influence the work reported in this paper.

Data availability

Data will be made available on request.

Acknowledgements

This work is jointly supported by the China National Funds for Distinguished Young Scientists (No. 51925104), and the National Natural Science Foundation of China (Nos. 51871162, and 52173251), NSFC-Guangdong Province Joint Program (Key program no. U21A2084).

Appendix A. Supporting information

Supplementary data associated with this article can be found in the online version at doi:10.1016/j.apcatb.2022.121701.

References

- [1] Y. Cui, J. Zhang, H. He, G. Qian, Photonic functional metal-organic frameworks, Chem. Soc. Rev. 47 (2018) 5740–5785.
- [2] J. Li, H. Huang, W. Xue, K. Sun, X. Song, C. Wu, L. Nie, Y. Li, C. Liu, Y. Pan, H. L. Jiang, D. Mei, C. Zhong, Self-adaptive dual-metal-site pairs in metal-organic frameworks for selective CO₂ photoreduction to CH₄, Nat. Catal. 4 (2021) 719–729.
- [3] Q. Zheng, X. Liu, Y. Zheng, K.W.K. Yeung, Z. Cui, Y. Liang, Z. Li, S. Zhu, X. Wang, S. Wu, The recent progress on metal—organic frameworks for phototherapy, Chem. Soc, Rev. 50 (2021) 5086–5125.
- [4] Z. Jiang, X. Xu, Y. Ma, H.S. Cho, D. Ding, C. Wang, J. Wu, P. Oleynikov, M. Jia, J. Cheng, Y. Zhou, O. Terasaki, T. Peng, L. Zan, H. Deng, Filling metal–organic framework mesopores with TiO₂ for CO₂ photoreduction, Nature 586 (2020) 549–554
- [5] J. Li, L. He, Q. Liu, Y. Ren, H. Jiang, Visible light-driven efficient palladium catalyst turnover in oxidative transformations within confined frameworks, Nat. Commun. 13 (2022) 928.
- [6] M. Taniguchi, J.S. Lindsey, Synthetic Chlorins, Possible surrogates for chlorophylls, prepared by derivatization of porphyrins, Chem. Rev. 117 (2017) 344–535.
- [7] H. Hu, Z. Wang, L. Cao, L. Zeng, C. Zhang, W. Lin, C. Wang, Metal-organic frameworks embedded in a liposome facilitate overall photocatalytic water splitting, Nat. Chem. 13 (2021) 358–366.
- [8] G. Chakraborty, I.H. Park, R. Medishetty, J.J. Vittal, Two-dimensional metalorganic framework materials: synthesis, structures, properties and applications, Chem. Rev. 121 (2021) 3751–3891.
- [9] J. Li, S. Song, J. Meng, L. Tan, X. Liu, Y. Zheng, Z. Li, K.W.K. Yeung, Z. Cui, Y. Liang, S. Zhu, X. Zhang, S. Wu, 2D MOF periodontitis photodynamic ion therapy, J. Am. Chem. Soc. 143 (2021) 15427–15439.
- [10] W. Xu, J. Wang, H. Yu, P. Liu, G.R. Zhang, H. Huang, D. Mei, Size-dependent electron injection over sensitized semiconductor heterojunctions for enhanced photocatalytic hydrogen production, Appl. Catal., B 308 (2022), 121218.
- [11] S. Wu, Z. Li, M.Q. Li, Y. Diao, F. Lin, T. Liu, J. Zhang, P. Tieu, W. Gao, F. Qi, X. Pan, Z. Xu, Z. Zhu, A.K.Y. Jen, 2D metal-organic framework for stable perovskite solar cells with minimized lead leakage, Nat. Nanotechnol. 15 (2020) 934–940.
- [12] M. Pan, W.M. Liao, S.Y. Yin, S.S. Sun, C.Y. Su, Single-phase white-light-emitting and photoluminescent color-tuning coordination assemblies, Chem. Rev. 118 (2018) 8889–8935.
- [13] M. Fumanal, A. Ortega-Guerrero, K.M. Jablonka, B. Smit, I. Tavernelli, Charge separation and charge carrier mobility in photocatalytic metal-organic frameworks. Adv. Funct. Mater. 30 (2020). 2003792.
- [14] Z.B. Fang, T.T. Liu, J. Liu, S. Jin, X.P. Wu, X.Q. Gong, K. Wang, Q. Yin, T.F. Liu, R. Cao, H.C. Zhou, Boosting interfacial charge-transfer kinetics for efficient overall co₂ photoreduction via rational design of coordination spheres on metal–organic frameworks. J. Am. Chem. Soc. 142 (2020) 12515–12523.
- [15] P. Cai, M. Xu, S.S. Meng, Z. Lin, T. Yan, H.F. Drake, P. Zhang, J. Pang, Z.Y. Gu, H. C. Zhou, Precise spatial-designed metal-organic-framework nanosheets for efficient energy transfer and photocatalysis, Angew. Chem., Int. Ed. 60 (2021) 27258–27263.

- [16] Y. Zhao, L. Zhang, J. Liu, K. Adair, F. Zhao, Y. Sun, T. Wu, X. Bi, K. Amine, J. Lu, X. Sun, Atomic/molecular layer deposition for energy storage and conversion, Chem. Soc. Rev. 50 (2021) 3889–3956.
- [17] J. Cai, X. Han, X. Wang, X. Meng, Atomic layer deposition of two-dimensional layered materials: processes, growth mechanisms, and characteristics, Matter 2 (2020) 587–630.
- [18] X. Yang, A.B.F. Martinson, J.W. Elam, L. Shao, S.B. Darling, Water treatment based on atomically engineered materials: atomic layer deposition and beyond, Matter 4 (2021) 3515–3548.
- [19] S. Corby, R.R. Rao, L. Steier, J.R. Durrant, The kinetics of metal oxide photoanodes from charge generation to catalysis, Nat. Rev. Mater. 6 (2021) 1136–1155.
- [20] Y. Li, W. Zhang, J. Niu, Y. Chen, Mechanism of photogenerated reactive oxygen species and correlation with the antibacterial properties of engineered metal-oxide nanoparticles, ACS Nano 6 (2012) 5164–5173.
- [21] J. Li, L. Ma, Z. Li, X. Liu, Y. Zheng, Y. Liang, C. Liang, Z. Cui, S. Zhu, S. Wu, Oxygen vacancies-rich heterojunction of Ti₃C₂/BiOBr for photo-excited antibacterial textiles, Small 18 (2022), 2104448.
- [22] M. Zhao, Y. Wang, Q. Ma, Y. Huang, X. Zhang, J. Ping, Z. Zhang, Q. Lu, Y. Yu, H. Xu, Y. Zhao, H. Zhang, Ultrathin 2D metal—organic framework nanosheets, Adv. Mater. 27 (2015) 7372–7378.
- [23] Y. Zhao, N. Kornienko, Z. Liu, C. Zhu, S. Asahina, T.-R. Kuo, W. Bao, C. Xie, A. Hexemer, O. Terasaki, P. Yang, O.M. Yaghi, Mesoscopic constructs of ordered and oriented metal-organic frameworks on plasmonic silver nanocrystals, J. Am. Chem. Soc. 137 (2015) 2199–2202.
- [24] H. Ang, L. Hong, Polycationic polymer-regulated assembling of 2D MOF nanosheets for high-performance nanofiltration, ACS Appl. Mater. Interfaces 9 (2017) 28079–28088.
- [25] F. Yang, W. Hu, C. Yang, M. Patrick, A.L. Cooksy, J. Zhang, J.A. Aguiar, C. Fang, Y. Zhou, Y.S. Meng, J. Huang, J. Gu, Tuning internal strain in metal-organic frameworks via vapor phase infiltration for CO₂ reduction, Angew. Chem., Int. Ed. 59 (2020) 4572–4580.
- [26] H.B. Khosravi, R. Rahimi, M. Rabbani, A. Maleki, A. Mollahosseini, Design, Facile Synthesis and characterization of porphyrin-zirconium-ferrite@SiO₂ core-shell and catalytic application in cyclohexane oxidation, Silicon 13 (2021) 451–465.

- [27] A.P. Balan, S. Radhakrishnan, C.F. Woellner, S.K. Sinha, L. Deng, C. de los Reyes, B. M. Rao, M. Paulose, R. Neupane, A. Apte, V. Kochat, R. Vajtai, A.R. Harutyunyan, C.W. Chu, G. Costin, D.S. Galvao, A.A. Martí, P.A. van Aken, O.K. Varghese, C. S. Tiwary, A.M.M.R. lyer, P.M. Ajayan, , Exfoliation of a non-van der Waals material from iron ore hematite, Nat. Nanotechnol. 13 (2018) 602–609.
- [28] J. Li, X. Liu, L. Tan, Y. Liang, Z. Cui, X. Yang, S. Zhu, Z. Li, Y. Zheng, K.W.K. Yeung, X. Wang, S. Wu, Light-activated rapid disinfection by accelerated charge transfer in red phosphorus/ZnO heterointerface, Small Methods 3 (2019), 1900048.
- [29] E.P. Kamphaus, N. Shan, J.C. Jones, A.B.F. Martinson, L. Cheng, Selective hydration of rutile TiO₂ as a strategy for site-selective atomic layer deposition, ACS Appl. Mater. Interfaces 14 (2022) 21585–21595.
- [30] M.A. Rajora, J.W.H. Lou, G. Zheng, Advancing porphyrin's biomedical utility via supramolecular chemistry, Chem. Soc. Rev. 46 (2017) 6433–6469.
- [31] Z.W. Jiang, Y.C. Zou, T.T. Zhao, S.J. Zhen, Y.F. Li, C.Z. Huang, Controllable synthesis of porphyrin-based 2D lanthanide metal-organic frameworks with thickness- and metal-node-dependent photocatalytic performance, Angew. Chem., Int. Ed. 59 (2020) 3300–3306.
- [32] G. Xu, H. Zhang, J. Wei, H.X. Zhang, X. Wu, Y. Li, C. Li, J. Zhang, J. Ye, Integrating the g-C₃N₄ nanosheet with B–H bonding decorated metal–organic framework for CO₂ activation and photoreduction, ACS Nano 12 (2018) 5333–5340.
- [33] S. Xie, Y. Li, B. Sheng, W. Zhang, W. Wang, C. Chen, J. Li, H. Sheng, J. Zhao, Self-reconstruction of paddle-wheel copper-node to facilitate the photocatalytic CO₂ reduction to ethane, Appl. Catal., B 310 (2022), 121320.
- [34] Y. Zhao, Y. Liu, Z. Wang, Y. Ma, Y. Zhou, X. Shi, Q. Wu, X. Wang, M. Shao, H. Huang, Y. Liu, Z. Kang, Carbon nitride assisted 2D conductive metal-organic frameworks composite photocatalyst for efficient visible light-driven H2O2 production, Appl. Catal., B 289 (2021), 120035.
- [35] Z.Q. Li, G.L. Zhu, R.J. Mo, M.Y. Wu, X.L. Ding, L.Q. Huang, Z.Q. Wu, X.H. Xia, Light-enhanced osmotic energy harvester using photoactive porphyrin metal-organic framework membranes, Angew. Chem. Int. Ed. 61 (2022), e202202698
- [36] D. Yang, S. Zuo, H. Yang, Y. Zhou, Q. Lu, X. Wang, Tailoring layer number of 2D porphyrin-based MOFs towards photocoupled electroreduction of CO₂, Adv. Mater. 34 (2022), 2107293.